AIAA JOURNAL
Vol. 48, No. 2, February 2010

Curved Boundary Treatments for the Discontinuous Galerkin Method Applied to Aeroacoustic Propagation

Thomas Toulorge* and Wim Desmet†
Katholieke Universiteit Leuven, B-3001 Heverlee, Belgium

DOI: 10.2514/1.45353

A discontinuous Galerkin method is applied to unstructured grids to simulate aeroacoustic propagation, modeled by the linearized Euler equations. On triangular and tetrahedral elements with straight edges, the quadrature-free form of the discontinuous Galerkin method is used. In addition to the classical linear treatment of wall boundaries, two treatments involving a second-order representation of the geometry are presented. The simulation of acoustic scattering problems shows that the linear treatment can limit the accuracy at high order, and demonstrates how the boundary treatment involving curved elements overcomes this restriction. The benefits of higher-order treatments are also assessed for more realistic geometries, namely a high-lift airfoil and an elliptical muffler.

Nomenclature

$\mathbf{F}$	=	vector of fluxes
$\mathbf{F_R}$	=	vector of Riemann fluxes
$\mathbf{K}$	=	stiffness matrix
$\mathbf{M}$	=	mass matrix
p	=	pressure
$\mathbf{q}$	=	vector of variables
t	=	time
u	=	velocity
x	=	Cartesian coordinate in physical space
Δ	=	reference element
Ω	=	element in physical space
$\partial\Delta$	=	reference element boundary
$\partial\Omega$	=	element boundary in physical space
ξ	=	Cartesian coordinate in reference space
ρ	=	density
φ	=	basis function

Subscripts

i	=	edge index in an element
j, k	=	basis function indices
r	=	Cartesian coordinate index in physical space
s	=	Cartesian coordinate index in reference space
0	=	mean flow quantity

I. Introduction

THE computation of sound propagation in a nonuniform flow is an essential part of computational aeroacoustics (CAA). This problem, which can be modeled by the linearized Euler equations (LEE), requires the numerical scheme to produce very low dissipation and dispersion, as acoustic waves may propagate over long distances without attenuation due to viscous effects. To be of practical utility, the method shall also be able to handle complex geometries through the use of unstructured grids.

Among the methods that fulfill these requirements, the discontinuous Galerkin method (DGM) is a promising candidate. It was introduced in the early 1970s [1,2] to simulate neutron transport and has been applied to numerous equations since then, particularly in the fields of electromagnetism and fluid dynamics. Just as the continuous finite element method (FEM), it consists of representing the local quantities in each element of the grid by a projection on a polynomial basis, and applying the Galerkin procedure to the governing Partial Differential Equation. In contrast to traditional FEM, where the continuity of variables between elements is imposed, DGM allows the solution to be discontinuous at element boundaries. Similarly to finite volume methods, conservation is enforced through the use of a flux at element boundaries, where a Riemann problem is solved. This construction features an arbitrary order of accuracy, which only depends on the order of the underlying polynomial basis while maintaining an extreme compactness. The only nonlocal information used in the scheme comes from the communication between an element and its neighbors. Along with the ability to handle unstructured grids and the straightforward formulation of boundary conditions through the flux formulation, these properties are clear advantages over the finite difference (FD) schemes traditionally used to solve the LEE for CAA applications. However, DGM has been criticized for two reasons that make it computationally expensive compared with FD methods: discontinuous solutions require extra degrees of freedom, and the method involves integration of higher-order functions, which are traditionally carried out through quadrature. The latter is palliated by Atkins and Shu [3] by introducing the quadrature-free form of DGM, which consists of mapping all elements in the physical domain onto a single reference element for which the integration of base function products is precomputed. However, this technique is subject to certain constraints on the geometry of physical elements (e.g., straight edges for triangles or flat faces for tetrahedra).

Several authors have investigated the application of DGM to wave propagation problems. In particular, the behavior of DGM with respect to dissipation and dispersion has been well studied by means of theory and numerical experiments [4–7]. The influence of h and p refinement on the accuracy of DGM [8,9], as well as the discretization error on different kinds of grids [10,11], were investigated. Several authors report the successful application of DGM to Maxwell's equations [12] and to aeroacoustic problems [13–16]. However, these works do not include the study of the error that is due to the discretization of the geometry.

In the framework of the nonlinear Euler equations, the necessity of a higher-order treatment of curved wall boundaries was put in evidence by Bassi and Rebay [17], and is now generally accepted [18]. [17,18] suggest that the accuracy mainly depends on the correct representation of the normals to the geometry when dealing with 2-D Euler flows. However, this might not be the case with acoustic propagation problems. Concerning the LEE, Atkins reported the use

Presented as Paper 3176 at the 15th AIAA/CEAS Aeroacoustics Conference, Miami, FL, 11–13 May 2009; received 8 May 2009; revision received 18 October 2009; accepted for publication 8 November 2009.

*Ph.D. Student, Department of Mechanical Engineering, Celestijnenlaan 300. Member AIAA.

†Professor, Department of Mechanical Engineering, Celestijnenlaan 300.

of higher-order geometry description and its benefits on problems of acoustic scattering [19].

In the present work, DGM is applied to the LEE to simulate aeroacoustic propagation on triangular and tetrahedral grids, with the objective of studying the influence of boundary treatment for curved walls. Academic problems of acoustic scattering in 2D and 3D are used to show how the linear treatment of wall boundaries limits the accuracy. The improvement brought by two different boundary treatments based on higher-order geometry representation are evaluated for these problems. The benefits of higher-order boundary treatments are also applied to more realistic geometries, with the computation of sound scattering by a high-lift airfoil and the analysis of transmission loss in an elliptical muffler. In all test cases presented in this work no mean flow is applied, so that results are restricted to pure acoustics to isolate the accuracy and stability issues raised by boundary treatments.

The outline of this paper is the following: the numerical method is described in Sec. II, and the results of the test problems are discussed in Sec. III. Conclusions are drawn in Sec. IV.

II. Method

The approach taken here is based on the work of Reymen [20], who uses a nodal DGM on tetrahedral and hexahedral grids, combined with a low-storage fourth-order-accurate Runge–Kutta scheme [21] for time integration. This method was successfully applied to the LEE in the framework of aeroacoustic simulations [22]. In the present work, this approach is extended to curved triangular and tetrahedral elements to model curved wall boundaries, with the purpose of overcoming the limitations of linear geometry treatment that are put in evidence in Sec. III. For the sake of simplicity, this section will describe the 2-D method; generalization to 3D is straightforward.

A. Governing Equations

The governing equations are the linearized Euler equations, which are capable of solving acoustic propagation in nonuniform flows

$$\frac{\partial \mathbf{q}}{\partial t} + \frac{\partial \mathbf{F_r}}{\partial x_r} + \mathbf{C}\mathbf{q} = \mathbf{s} \tag{1}$$

where

$$\mathbf{q} = \begin{bmatrix} \rho \\ \rho_0 u_1 \\ \rho_0 u_2 \\ p \end{bmatrix}$$

$$\mathbf{F_r} = \mathbf{A_r}\mathbf{q} = \begin{bmatrix} u_{0r} & \delta_{1r} & \delta_{2r} & 0 \\ 0 & u_{0r} & 0 & \delta_{1r} \\ 0 & 0 & u_{0r} & \delta_{2r} \\ 0 & \frac{\gamma p_0}{\rho_0}\delta_{1r} & \frac{\gamma p_0}{\rho_0}\delta_{2r} & u_{0r} \end{bmatrix} \mathbf{q}$$

$$\mathbf{C} = \begin{bmatrix} 0 & 0 & 0 & 0 \\ u_{0r}\frac{\partial u_{01}}{\partial x_r} & \frac{\partial u_{01}}{\partial x_1} & \frac{\partial u_{01}}{\partial x_2} & 0 \\ u_{0r}\frac{\partial u_{02}}{\partial x_r} & \frac{\partial u_{02}}{\partial x_1} & \frac{\partial u_{02}}{\partial x_2} & 0 \\ 0 & \frac{(1-\gamma)}{\rho_0}\frac{\partial p_0}{\partial x_1} & \frac{(1-\gamma)}{\rho_0}\frac{\partial p_0}{\partial x_2} & (\gamma-1)\frac{\partial u_{0r}}{\partial x_r} \end{bmatrix}$$

Here r is one of the two Cartesian coordinates ($x_1 \equiv x, x_2 \equiv y$) on which Einstein's summation convention is used; $\mathbf{s}$ is the acoustic source vector; (ρ, u_1, u_2, p) are, respectively, the acoustic perturbations in density, x velocity, y velocity, and pressure, and $(\rho_0, u_{10}, u_{20}, p_0)$ are the corresponding quantities for the mean flow; γ is the heat capacity ratio and δ_{ij} is the Kronecker delta. The term $\mathbf{Cq}$ accounts for nonuniform mean flow effects, and is not considered in this work.

B. Spatial Discretization

In this work, DGM is applied to unstructured triangular meshes. The computational domain is paved with straight-edge triangles, on which the quadrature-free form of DGM is applied. Optionally, elements and edges with second-order shape that require the use of quadrature can be employed near curved wall boundaries.

1. Formulation

For each element Ω of the grid, a basis $\mathcal{B} = \{\varphi_j, j = 1 \dots N_p\}$ is defined, in which the components φ_j are polynomials of order p supported by Ω, with $N_p = \frac{(p+1)(p+2)}{2}$ for triangular elements. An approximation $\mathbf{q}^\Omega$ of the vector of variables $\mathbf{q}$ on Ω is obtained by a projection on this basis

$$\mathbf{q}^\Omega = \sum_{j=1}^{N_p} \mathbf{q}_j^\Omega \varphi_j$$

Applying the Galerkin procedure to Eq. (1) with $\mathbf{s} = 0$ and $\mathbf{C} = 0$ and using the Green–Gauss theorem results in

$$\int_\Omega \varphi_k \sum_{j=1}^{N_p} \frac{\partial \mathbf{q}_j^\Omega}{\partial t}\varphi_j \,\mathrm{d}\Omega - \int_\Omega \frac{\partial \varphi_k}{\partial x_r} \sum_{j=1}^{N_p} \mathbf{F}_{\mathbf{r}j}^\Omega \varphi_j \,\mathrm{d}\Omega + \int_{\partial\Omega} \varphi_k \sum_{j=1}^{N_p} \mathbf{F}_{\mathbf{R}j}^{\partial\Omega}\varphi_j \,\mathrm{d}\partial\Omega = 0, \qquad k = 1 \dots N_p \tag{2}$$

where $\mathbf{F}_\mathbf{r}^\Omega$ is a projection of $\mathbf{F_r}$ on $\mathcal{B}$, and $\mathbf{F}_\mathbf{R}^{\partial\Omega}$ is a projection on $\mathcal{B}$ of the Riemann flux computed on the element boundary $\partial\Omega$ as

$$\mathbf{F}_\mathbf{R}^{\partial\Omega} = \frac{1}{2}[(\mathbf{F}_\mathbf{r}^\Omega + \mathbf{F}_\mathbf{r}^{\Omega'})n_r - \alpha(\mathbf{q}^{\Omega'} - \mathbf{q}^\Omega)] \tag{3}$$

α is the maximum eigenvalue of $\frac{\partial \mathbf{F}}{\partial \mathbf{q}}$, n_r is the r component of the local outgoing normal to the boundary $\partial\Omega$, $\mathbf{q}^{\Omega'}$ and $\mathbf{F}_\mathbf{r}^{\Omega'}$ are the equivalents of $\mathbf{q}^\Omega$ and $\mathbf{F}_\mathbf{r}^\Omega$, respectively, in the element Ω' locally sharing $\partial\Omega$ with Ω. Following the quadrature-free form of DGM [3], all elements in the physical domain can then be mapped onto a single reference element Δ

$$\mathcal{M}^\Omega\colon \Delta \to \Omega \qquad (\xi_1, \xi_2) \mapsto (x_1, x_2)$$

The Jacobian matrix of $\mathcal{M}^\Omega$ is defined as $J_{ij}^\Omega = \frac{\partial x_i}{\partial \xi_j}$, and the change of coordinates in Eq. (2) yields

$$\int_\Delta \varphi_k \sum_{j=1}^{N_p} \frac{\partial \mathbf{q}_j^\Omega}{\partial t}\varphi_j |J^\Omega| \,\mathrm{d}\Delta - \int_\Delta (J^\Omega)_{\mathrm{sr}}^{-1} \frac{\partial \varphi_k}{\partial \xi_s} \sum_{j=1}^{N_p} \mathbf{F}_{\mathbf{r}j}^\Omega \varphi_j |J^\Omega| \,\mathrm{d}\Delta + \sum_{i=1}^{3} \int_{\partial\Delta_i} \varphi_k \sum_{j=1}^{N_p} \mathbf{F}_{\mathbf{R}j}^{\partial\Omega}\varphi_j |J^{\partial\Omega_i}| \,\mathrm{d}\partial\Delta_i = 0, \qquad k = 1 \dots N_p \tag{4}$$

where $J^{\partial\Omega_i}$ is the Jacobian matrix of the mapping of the edge $\partial\Omega_i$ of Ω on the corresponding edge $\partial\Delta_i$ of Δ. Equation (4) can then be rewritten in a matrix form

$$\mathbf{M}^\Omega \frac{\partial \mathbf{q}^\Omega}{\partial t} - \mathbf{K}_\mathbf{r}^\Omega \mathbf{F}_\mathbf{r}^\Omega + \sum_{i=1}^{3} \mathbf{M}^{\partial\Omega_i} \mathbf{F}_\mathbf{R}^{\partial\Omega_i} = 0 \tag{5}$$

with

$$\mathbf{M}_{kj}^\Omega = \int_\Delta \varphi_k \varphi_j |J^\Omega| \,\mathrm{d}\Delta$$

$$(\mathbf{K}_\mathbf{r}^\Omega)_{kj} = \int_\Delta (J^\Omega)_{\mathrm{sr}}^{-1} \frac{\partial \varphi_k}{\partial \xi_s} \varphi_j |J^\Omega| \,\mathrm{d}\Delta \tag{6}$$

$$\mathbf{M}_{kj}^{\partial\Omega_i} = \int_{\partial\Delta_i} \varphi_k \varphi_j |J^{\partial\Omega_i}| \,\mathrm{d}\partial\Delta_i$$

In this work, the basis functions φ_j are Lagrange polynomials based on a nodal set that reduces to Lagrange–Gauss–Lobatto points on the edges [23]. Thus, $\mathcal{B}$ reduces to a basis of 1-D polynomials on $\partial\Omega_i$, which can be used to store lower-rank matrices for $\mathbf{M}^{\partial\Omega_i}$ and

$\mathbf{F}_{\mathbf{R}}^{\partial\Omega_i}$. Integrals are computed on a polynomial basis that is orthogonal in Δ, following the work of Hesthaven and Warburton [12].

2. Elements with Straight Edges

On elements that are triangles with straight edges, J^Ω and $J^{\partial\Omega_i}$ are constant over Δ and $\partial\Delta_i$, respectively, so that they can be taken out of the integrals in Eq. (6)

$$\mathbf{M}^\Omega = |J^\Omega|\mathbf{M}^\Delta \qquad \mathbf{K}_{\mathbf{r}}^\Omega = (J^\Omega)^{-1}_{\mathrm{sr}}|J^\Omega|\mathbf{K}_{\mathbf{s}}^\Delta \qquad \mathbf{M}^{\partial\Omega_i} = |J^{\partial\Omega_i}|\mathbf{M}^{\partial\Delta_i}$$

with

$$\begin{aligned}\mathbf{M}_{kj}^\Delta &= \int_\Delta \varphi_k\varphi_j \,\mathrm{d}\Delta \\ (\mathbf{K}_{\mathbf{s}}^\Delta)_{kj} &= \int_\Delta \frac{\partial\varphi_k}{\partial\xi_s}\varphi_j \,\mathrm{d}\Delta \\ \mathbf{M}_{kj}^{\partial\Delta_i} &= \int_{\partial\Delta_i} \varphi_k\varphi_j \,\mathrm{d}\partial\Delta_i \end{aligned} \tag{7}$$

The memory storage for each element and edge thus reduces to the Jacobian terms, given that $\mathbf{M}^\Delta$, $\mathbf{K}_{\mathbf{s}}^\Delta$, and $\mathbf{M}^{\partial\Delta_i}$ can be precomputed. The use of an orthogonal basis in Δ, for which a transformation from $\mathcal{B}$ is defined, allows an easy analytical computation of matrices in Eq. (7).

3. Curved Elements

To improve the representation of curved wall boundaries, elements with second-order shape can be used in the vicinity of the geometry. In this case, $\mathcal{M}^\Omega$ is of order 2 and extra points are needed to completely describe the shape of the element, in addition to the vertices of the simplex. Consequently, J^Ω and $J^{\partial\Omega_i}$ are no longer constant over Ω and $\partial\Omega_i$, respectively, and they cannot be taken out of the integrals in Eq. (6), which has two implications.

1. Integration in Eq. (6) requires quadrature. In the present work, Gauss–Legendre quadrature rules are used to compute the matrices. Care is taken to choose rules of sufficiently high order to correctly integrate the products of polynomials that form the integrands.

2. Integrals in Eq. (6) cannot be precomputed, so that $\mathbf{M}^\Omega$ and $\mathbf{K}_{\mathbf{r}}^\Omega$ are calculated and stored in memory for each element Ω of the grid, as well as $\mathbf{M}^{\partial\Omega_i}$ for each edge $\partial\Omega_i$. For these elements and edges, the cost in memory is thus much higher than with the quadrature-free technique described in Sec. II.B.2.

The use of curved edges also implies that the components n_r of the normal to $\partial\Omega_i$ in Eq. (3) are not constant. Thus, the projection of the Riemann flux on $\mathcal{B}$ results in a truncation. As $\partial\Omega_i$ is described by a quadratic polynomial, the scalar product $(\mathbf{F}_{\mathbf{r}}^\Omega + \mathbf{F}_{\mathbf{r}}^{\Omega'})n_r$ is of order $p+1$, whereas $\mathbf{F}_{\mathbf{R}}^{\partial\Omega}$ is of order p. To prevent truncation, the terms in Eq. (3) have to be integrated separately and Eq. (5) then becomes

$$\mathbf{M}^\Omega \frac{\partial\mathbf{q}^\Omega}{\partial t} - \mathbf{K}_{\mathbf{r}}^\Omega\mathbf{F}_{\mathbf{r}}^\Omega + \sum_{i=1}^{3}\frac{1}{2}[\mathbf{M}_{\mathbf{r}}^{\partial\Omega_i}(\mathbf{F}_{\mathbf{r}}^\Omega + \mathbf{F}_{\mathbf{r}}^{\Omega'}) - \alpha\mathbf{M}^{\partial\Omega_i}(\mathbf{q}^{\Omega'} - \mathbf{q}^\Omega)] = 0$$

with

$$(\mathbf{M}_{\mathbf{r}})_{kj}^{\partial\Omega_i} = \int_{\partial\Delta_i} \varphi_k\varphi_j n_r |J^{\partial\Omega_i}| \,\mathrm{d}\partial\Delta_i$$

As a result, three matrices $\mathbf{M}_{\mathbf{1}}^{\partial\Omega_i}$, $\mathbf{M}_{\mathbf{2}}^{\partial\Omega_i}$, and $\mathbf{M}^{\partial\Omega_i}$ have to be stored in memory for each edge $\partial\Omega_i$ to avoid truncation, instead of one. Although computationally more demanding, this treatment is more accurate; therefore, all results presented in this work are obtained with nontruncated Riemann fluxes.

C. Boundary Treatment

All boundary conditions are enforced in a weak manner by prescribing the fluxes at boundary. Rigid walls are modeled by computing at each node of the boundary edge $\partial\Omega_i$ a modified flux that fulfills the condition

$$\mathbf{u}\cdot\mathbf{N} = 0 \quad \text{with} \quad \mathbf{u} = \begin{bmatrix} u_1 \\ u_2 \end{bmatrix}$$

and $\mathbf{N}$ being either the normal $\mathbf{n}$ to $\partial\Omega_i$, or the local normal $\mathbf{n_g}$ to the quadratically represented geometry. In this work, three different wall boundary treatments, illustrated in Fig. 1, are investigated.

1. $\partial\Omega_i$ is a straight edge and $\mathbf{N} = \mathbf{n}$. In this case the treatment of wall boundaries is fully linear, and the quadrature-free DGM is used, as described in Sec. II.B.2.

2. $\partial\Omega_i$ is a straight edge and $\mathbf{N} = \mathbf{n_g}$. As in the linear case, the quadrature-free DGM is used. This treatment, proposed in [17,18] as a cheap way to improve accuracy, will be hereafter referred to as mixed.

3. $\partial\Omega_i$ is a curved edge, in this case $\mathbf{N} = \mathbf{n} = \mathbf{n_g}$, and the treatment is fully quadratic. Integration over the edge $\partial\Omega_i$ and the adjacent element Ω is then performed by quadrature, as explained in Sec. II.B.3.

Lined walls are not considered in this paper.

D. Mesh Generation and Robustness

In this work, the software used for mesh generation is Gmsh [24], which is able to cope with second-order meshes following the process illustrated in Fig. 2. First-order grids, made out of straight elements, are generated in a classical manner as shown in Fig. 2a. From these, second-order grids are then produced by projecting the midpoint of boundary edges on the geometry, resulting in curved elements on the boundary. This second-order information can be used in conjunction with the original first-order grid for the mixed treatment.

The projection step is sometimes not sufficient to obtain satisfying second-order meshes. It can result in highly curved elements, which have an impact on the conditioning of DGM. Time steps must then be decreased to maintain the stability of computations. It can even lead to ill-shaped elements for which the mapping degenerates, as shown in Fig. 2b. DGM cannot be used with such grids.

Gmsh solves this problem by applying an additional smoothing step that consists in curving edges away from the boundary and involves edge swapping where necessary (see Fig. 2c). Nevertheless, curved elements remain confined in a region close to the geometry, and the elements in the rest of the computational domain can be considered as straight. As Gmsh outputs second-order information for the whole domain, a criterion based on a distortion measure γ is used to discriminate between straight and curved elements

$$\gamma = \min_\Omega\left(\frac{|J^\Omega|}{|J_0^\Omega|}, \frac{|J_0^\Omega|}{|J^\Omega|}\right)$$

where $|J_0^\Omega|$ is the Jacobian for the straight element corresponding to a second-order element Ω.

III. Results

The method described in Sec. II is applied to four test problems, with the objective of assessing the benefits of higher-order boundary treatments. As the interest of the mixed treatment appears to be limited in the two 2-D cases presented in Secs. III.A and III.B, it is not retained for evaluation in the 3-D problems. In all cases, coarse meshes are used in conjunction with high order to maximize the computational efficiency. A satisfying tradeoff between computational cost and accuracy is found at order $p = 7$ in most simulations, except for the muffler problem in Sec. III.D where lower order is needed.

A. Acoustic Scattering by a Cylinder

To assess the impact of wall boundary treatments, the problem Nr. 2, Category 1 of the Second CAA Workshop on Benchmark Problems [25] is studied. It consists of the scattering of a Gaussian

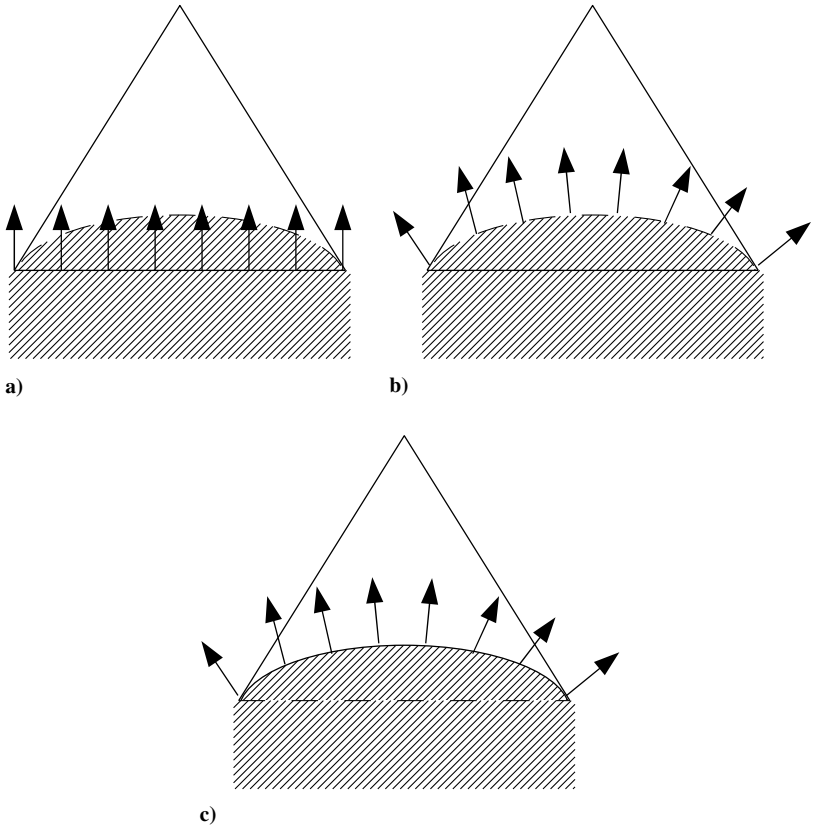

Fig. 1 Illustration of: a) the linear boundary treatment, b) the mixed boundary treatment, and c) the quadratic boundary treatment. The arrows represent the normals N used for prescribing the zero-normal-velocity condition, solid lines are the element boundaries on which the flux is integrated.

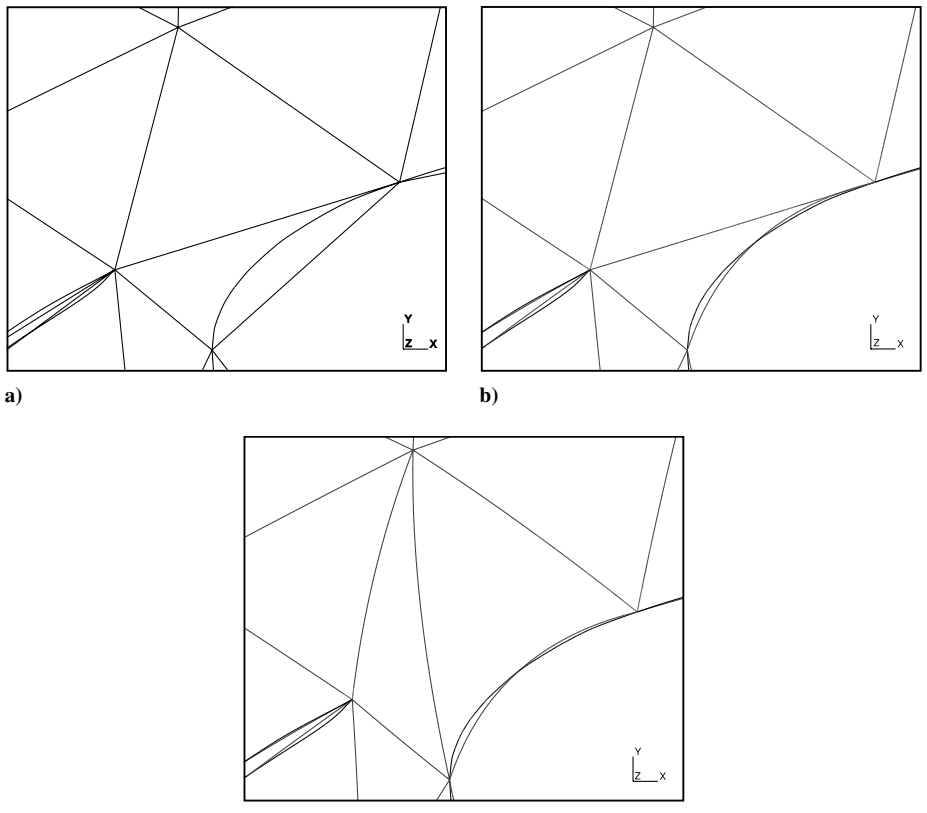

Fig. 2 Detail of the meshing process close to the leading edge of the high-lift airfoil presented in Sec. III.B: a) first-order mesh, b) primary second-order mesh, and c) smoothed second-order mesh.

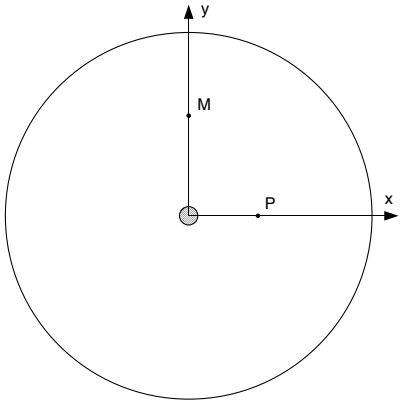

Fig. 3 Computational domain for the 2-D acoustic scattering problem. P(4,0) is the center of the pulse at initial time, M(0,5) is the point where the pressure is monotored.

pressure pulse by a cylinder. An analytical solution is available for this case. In addition to the results presented here, complementary data and a detailed discussion are available in [26].

The computational domain shown in Fig. 3 is a disc with a nondimensional diameter of 20, containing a cylinder of diameter 1 centered at the origin. The initial conditions consist of a Gaussian pulse located at point P(4,0)

$$p|_{t=0} = \rho|_{t=0} = e^{-(\ln 2)\frac{(x-4)^2+y^2}{0.2^2}} \qquad u_1|_{t=0} = u_2|_{t=0} = 0$$

The mean flow velocity is set to zero and characteristic-based nonreflecting boundary conditions are imposed in the far field. The order of the polynomial basis is set to $p = 7$. A set of grids is generated by progressively refining the discretization of the cylinder, while maintaining a constant element size in the far field. The grid characteristics are summarized in Table 1 and the nomenclature of test cases is explained in Table 2. The simulations are run until a nondimensional time of $t = 10$.

To assess the effect of geometry discretization and wall boundary treatment on the quality of the solution, the pressure is monitored at point (0, 5) and compared with the analytical solution. The reference solution features a first maximum at about $t = 6.3$, corresponding to the direct field, and a second maximum at $t = 8.2$, corresponding to the scattered field.

Table 1 Characteristics of grids used for the 2-D acoustic scattering problem

Grid name	Vertices on the cylinder	Vertices	Elements
C4	4	924	1738
C8	8	1373	2636
C12	12	1618	3122
C16	16	1877	3636
C18	18	2030	3940
C20	20	2153	4184

Table 2 Nomenclature of test cases for the 2-D acoustic scattering problem

Test case name	Grid name	Boundary treatment
C4L	C4	Linear
C4M	C4	Mixed
C4Q	C4	Quadratic
C8L	C8	Linear
C8M	C8	Mixed
C12L	C12	Linear
C16L	C16	Linear
C18L	C18	Linear
C20L	C20	Linear

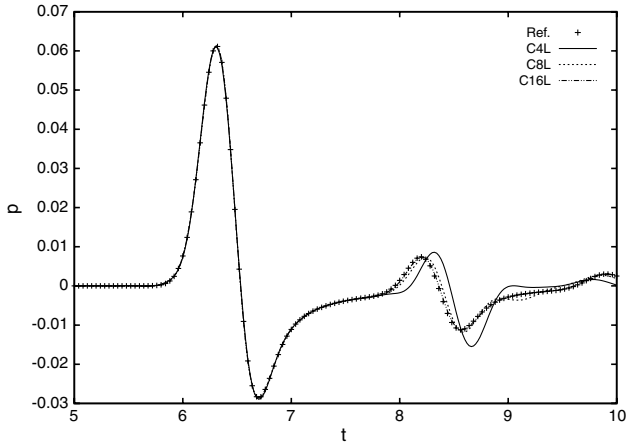

Fig. 4 Pressure at point (0,5) with linear boundary treatment on grids C4, C8, and C16 for the 2-D acoustic scattering problem.

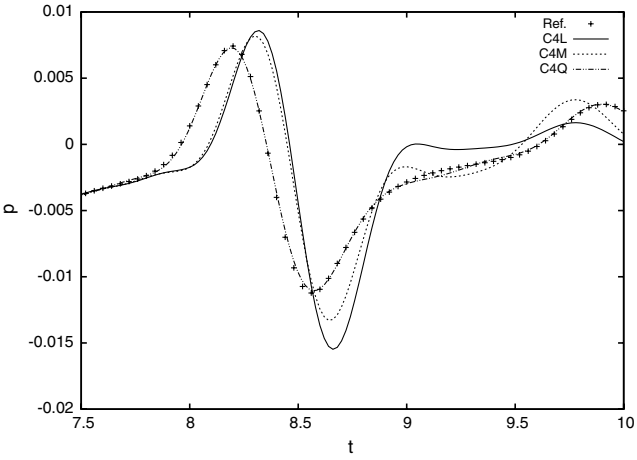

Fig. 5 Pressure at point (0,5) with different boundary treatments on grid C4 for the 2-D acoustic scattering problem.

Figure 4 shows the results of computations with the linear boundary treatment on grids C4, C8, and C16. In all cases, the direct pulse is well resolved. All grids are thus sufficiently refined to eliminate spurious dissipation and dispersion. However, a relatively large error in phase and amplitude appears in the scattered field on grid C4, and the results converge toward the reference data with geometry refinement. At $p = 7$, the accuracy is thus limited by the rough modeling of the cylinder.

Figure 5 shows the effect of higher-order boundary treatments on the scattered field with the coarsest grid C4. With this mesh, the mixed treatment does not significantly improve the accuracy (although it can prove useful on more refined grids, see [26]). The full quadratic treatment, on the other hand, yields a great improvement: as the cylinder geometry is well represented by the quadratic boundary, the phase error is suppressed. This is the reason why the solution for case C4Q is even more accurate than results obtained on refined grids with other boundary treatments, as shown in Table 3, which gives an overview of the accuracy of various simulations in the scattered field. One can note that 18 linear boundary elements (case C18L) are needed to achieve a similar accuracy as with 4 quadratic boundary elements (case C4Q), that is, 4.5 times more. This ratio cannot be generalized to other test problems, as it depends on how well the real geometry is approximated by second-order edges.

B. Sound Propagation around a High-Lift Airfoil

The influence of higher-order wall boundary treatments is assessed on the problem of a high-lift airfoil. The geometry is a three-element airfoil based on the RA16SC1 profile, with the slat and flap

Table 3 L_2 error in pressure at point (0,5) over the time interval [7.5, 10] for some cases of the 2-D acoustic scattering problem

Case name	Error
C4L	$2.78 \cdot 10^{-5}$
C4M	$1.83 \cdot 10^{-5}$
C4Q	$\mathbf{7.73 \cdot 10^{-8}}$
C8L	$2.63 \cdot 10^{-6}$
C8M	$1.46 \cdot 10^{-6}$
C12L	$4.51 \cdot 10^{-7}$
C16L	$1.28 \cdot 10^{-7}$
C18L	$\mathbf{7.77 \cdot 10^{-8}}$
C20L	$5.04 \cdot 10^{-8}$

deflected by 30 deg and 20 deg, respectively. The chord of the main element is 480 mm, and the computational domain is a disc of radius 1000 mm centered on a point P located close to the trailing edge. The acoustic excitation consists of a monopole source placed at point P, with the following source terms:

$$p_s = c_0^2 \rho_s = A \cdot \cos(2\pi f \cdot t) \cdot e^{-(\ln 2)\frac{(x-x_P)^2+(y-y_P)^2}{b^2}} \qquad u_{1s} = u_{2s} = 0$$

with

$$c_0 = 340 \text{ m} \cdot \text{s}^{-1} \qquad b = 3 \text{ mm} \qquad A = 1 \text{ Pa} \qquad f = 7816 \text{ Hz}$$

No mean flow is applied and characteristic-based nonreflecting boundary conditions are imposed at the outer limits of the computational domain shown in Fig. 6. Four different grids are generated: the element size remains constant in the far field, and the geometry is increasingly refined, particularly around curved parts of the geometry such as the slat, the leading edge of the main element, and the leading edge of the flap (see Fig. 7). The grid characteristics are summarized in Table 4. Order $p = 7$ is used for the six simulations whose parameters are listed in Table 5. The simulations are run until a periodic regime is reached. The results obtained with the finest grid are taken as reference data. Figure 8 shows the corresponding pressure field. The pressure is measured along a circle of radius 750 mm, centered at point P, to evaluate the influence of the boundary treatment on sound directivity.

The directivity of the sound pressure level for grids 1, 2, and 3 with the linear treatment can be seen in Fig. 9. The results obtained on the coarse grid 1 do not match the reference data well, especially in the $[\pi/2, \pi]$ and $[-\pi/2, 0]$ quadrants. Computations with a refined geometry discretization yield better results.

Figure 10 shows the effect of higher-order boundary treatments on the coarsest grid 1. Similarly to the 2-D cylinder problem, the mixed

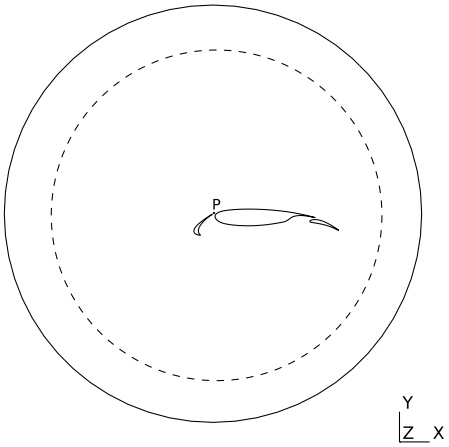

Fig. 6 Computational domain for the high-lift airfoil problem. Solid lines are the boundaries of the domain, the dashed line represents the surface where the pressure is monitored. Point P is the center of the domain where the acoustic monopole source is located.

Table 4 Characteristics of grids used for the high-lift airfoil case

Grid	Vertices	Elements
1	1819	3479
2	2481	4781
3	3397	6585
Ref.	6790	13239

Table 5 Computation parameters used for the high-lift airfoil case

Test case	Grid	Boundary treatment
1L	1	Linear
1M	1	Mixed
1Q	1	Quadratic
2L	2	Linear
3L	3	Linear
Ref.	Ref.	Linear

Table 6 Time step and approximate computational cost for each computation of the high-lift airfoil case

Test case	Time step	CPU time	Memory
1L	0.68	26 min	33.5 MB
1M	0.68	25 min	34.2 MB
1Q	0.64	28 min	36.0 MB
2L	0.67	35 min	45.2 MB
3L	0.36	1 h 31 min	61.4 MB

treatment does not significantly improve the accuracy, whereas the solution with the quadratic treatment is in excellent agreement with the reference data. Table 6 indicates the time step, as well as an estimation of the CPU time and memory requirements, for each computation. It can be noted that the quadratic treatment only has a minor additional computation cost in view of the improvement that it brings in accuracy. Although it achieves a lower accuracy than case 1Q, case 3L has a higher computation cost, due to the higher number of elements involved and the smaller time step, that is linked to the small element size. In grids 1 and 2, the smallest element size is limited to the size of gaps between wing elements, which explains the similar time steps with grids 1 and 2. Without such geometrical constraints, case 1Q would be even more advantageous in terms of CPU time because it would allow for a larger time step.

C. Acoustic Scattering by a Sphere

To verify the validity of curved boundary conditions in 3D, the problem of sound scattering by a sphere is studied. The computational domain is a ball with a nondimensional diameter of 20, containing a rigid sphere of diameter 2 centered at the origin. A monopole source is located at point (2, 0, 0), so that the source terms are

$$p_s = \rho_s = \cos(\omega t) \cdot e^{-(\ln 2)\frac{(x-2)^2+y^2+z^2}{b^2}} \qquad u_{1s} = u_{2s} = 0$$

where

$$\omega = \frac{5}{2}\pi \qquad b = 0.25$$

The mean flow velocity is set to zero and characteristic-based nonreflecting boundary conditions are imposed in the far field. The order of the polynomial basis is set to $p = 7$. The characteristics of the different grids used for this problem are summarized in Table 7. They feature the same element size in the far field, but differ in the

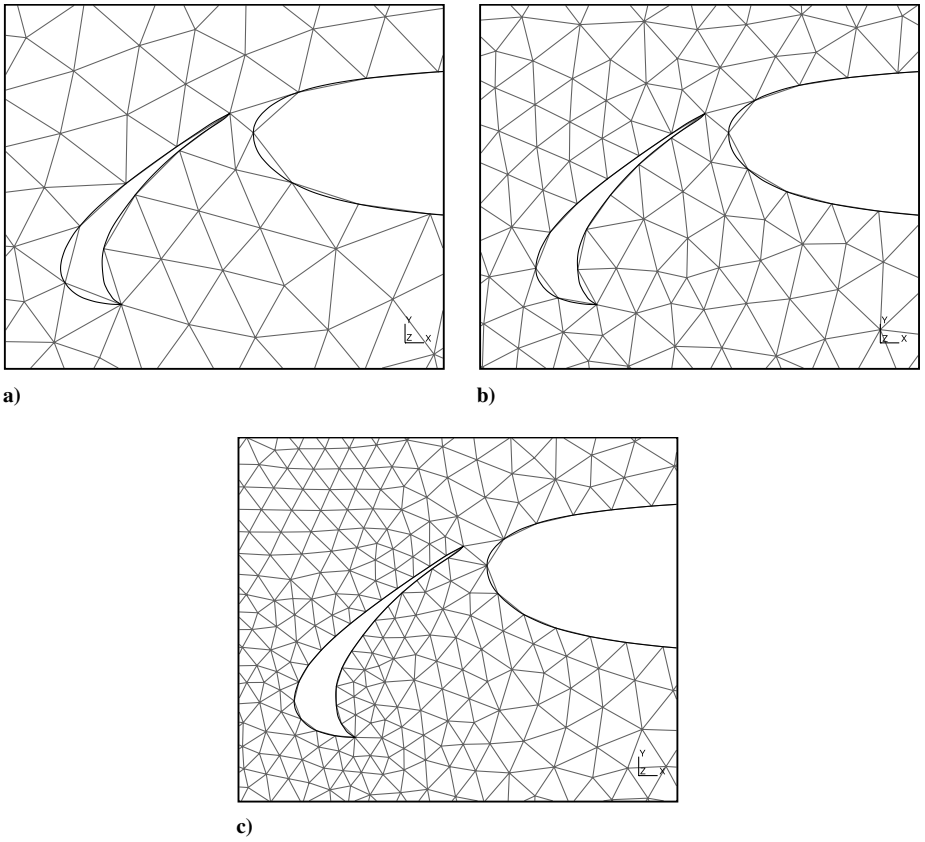

Fig. 7 Details of grids: a) grid 1, b) grid 2, and c) grid 3, close to the slat and the nose of the main element of the high-lift airfoil.

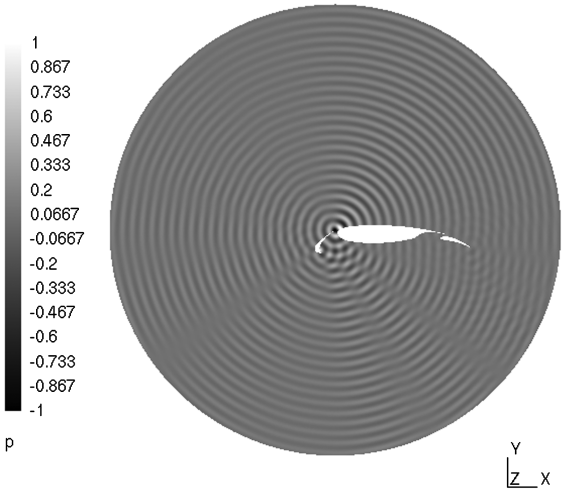

Fig. 8 Reference pressure field for the high-lift airfoil case.

discretization of the sphere. Table 8 explains the naming convention for the different configurations. The simulations are run until a periodic regime is reached. The pressure is measured along the circle $x^2 + y^2 = 25$ to check the effect of boundary treatment. The results on the finest grid with the linear boundary treatment are chosen as reference data.

Figure 11 shows the effect of grid refinement with the linear treatment. The computation with grids S8 and S32 exhibit a small error, whereas the results obtained with grid S94 are in good agreement with the reference data. Figure 12 shows that the quadratic boundary treatment suppresses the error with the coarse geometry discretization of grid S8. Table 9, which gives the time step and the approximate computational cost for each case, demonstrates that the improvement in accuracy brought by the quadratic boundary treatment comes for lower additional CPU time than with grid refinement. The higher computation time in case S92L is mainly due to a smaller time step, as the number of elements involved is similar to the other cases.

It should be mentioned that for this problem, increasing the frequency of the acoustic source would better illustrate the effect of the geometry discretization on sound scattering. Higher frequencies, however, were not investigated in this paper because of the large requirements in computation time.

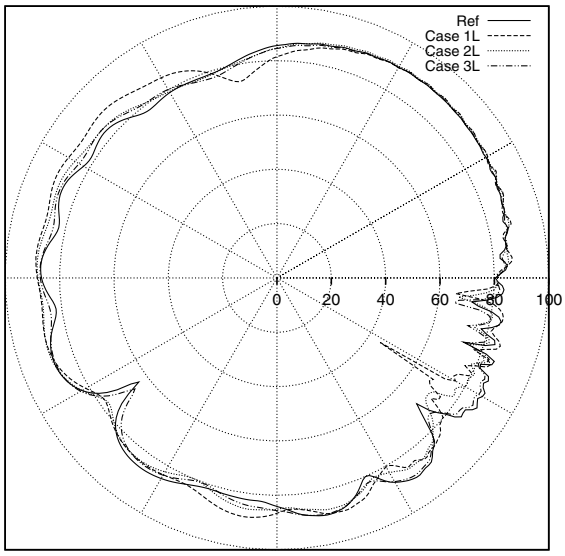

Fig. 9 Directivity of the sound pressure level (dB) for the high-lift airfoil case; effect of grid refinement.

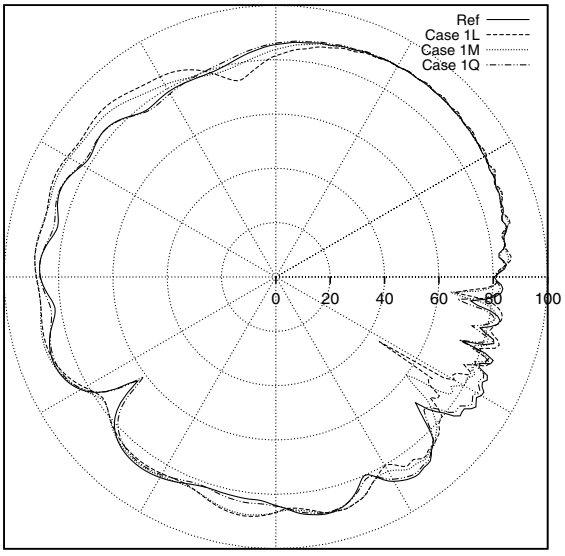

Fig. 10 Directivity of the sound pressure level (dB) for the high-lift airfoil case; comparison between the linear, mixed, and quadratic treatments on the coarsest grid.

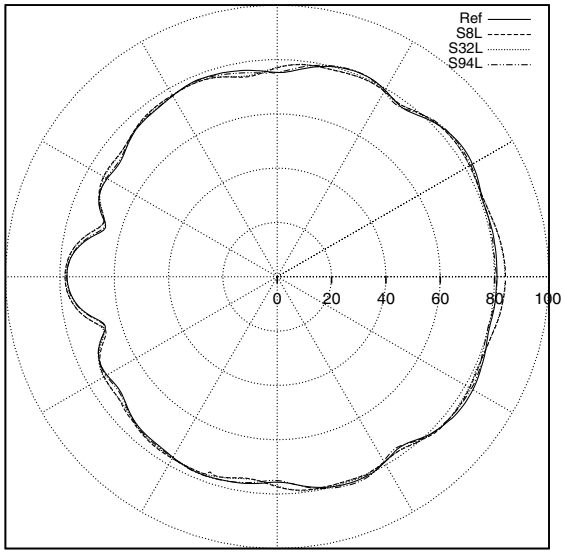

Fig. 11 Directivity of the sound pressure level (dB) for the 3-D scattering problem; effect of grid refinement.

D. Transmission Loss of a Muffler

The last test problem consists of an elliptical muffler with square inlet and outlet ducts, as shown in Fig. 13. The chamber has a length of 0.25 m, its elliptical section has a major semi-axis of $0.23/2$ m and a minor semi-axis of $0.13/2$ m. The reference solution for this configuration is computed by means of a modal expansion [27,28].

A plane pressure pulse is specified as the initial condition in the inlet duct

$$p|_{t=0} = \rho|_{t=0} = e^{-(\ell_n 2)\frac{(z+0.21)^2}{0.01^2}} \qquad u_1|_{t=0} = u_2|_{t=0} = 0$$

Table 7 Characteristics of grids used for the 3-D acoustic scattering problem

Grid	Faces on the sphere	Vertices	Elements
S8	8	4889	21553
S32	32	4854	21371
S94	94	5020	22272
Ref.	192	5636	25875

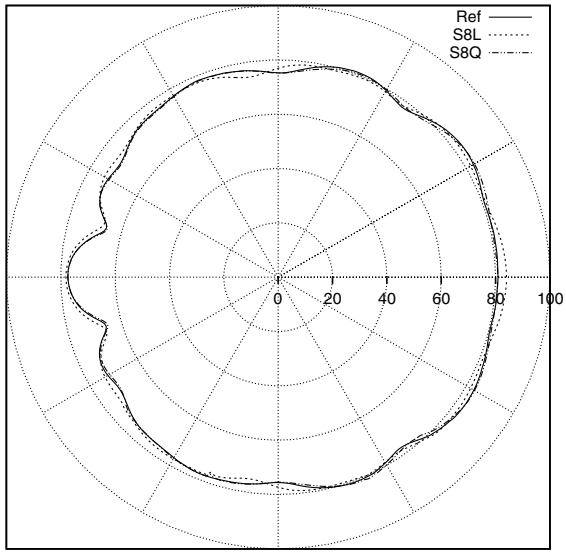

Fig. 12 Directivity of the sound pressure level (dB) for the 3-D scattering problem; effect of the boundary treatment.

No mean flow is applied and characteristic-based nonreflecting boundary conditions are applied in the inlet and outlet sections. The different grids, whose characteristics are given in Table 10, differ in the refinement of the chamber geometry. Order $p = 5$ is used in all cases except for grid 4, which is fine enough to use order $p = 4$ without significant dissipation or dispersion over the frequency range considered. An overview of the different configurations is given in Table 11.

The pressure is measured at two points P_1 and P_2 in the inlet duct and two points P_3 and P_4 in the outlet duct until time $t = 7.35 \cdot 10^{-2}$ s, when most of the acoustic energy introduced by the initial pulse has been propagated out of the system. After translation into the frequency domain by means of fast Fourier

Table 8 Computation parameters used for the 3-D acoustic scattering problem

Test case	Grid	Boundary treatment
S8L	1	Linear
S8Q	1	Quadratic
S32L	2	Linear
S94L	3	Linear
Ref.	Ref.	Linear

Table 9 Time step and approximate computational cost for each computation of the 3-D scattering problem

Test Case	Time Step	CPU Time	Memory
S8L	0.015	13 h 25 min	786.4 MB
S8Q	0.015	13 h 29 min	937.0 GB
S32L	0.015	13 h 18 min	779.9 MB
S94L	0.010	20 h 41 min	812.0 MB

Table 10 Characteristics of grids used for the muffler problem

Grid	Vertices	Elements
1	75	199
2	114	325
3	223	698
4	432	1322

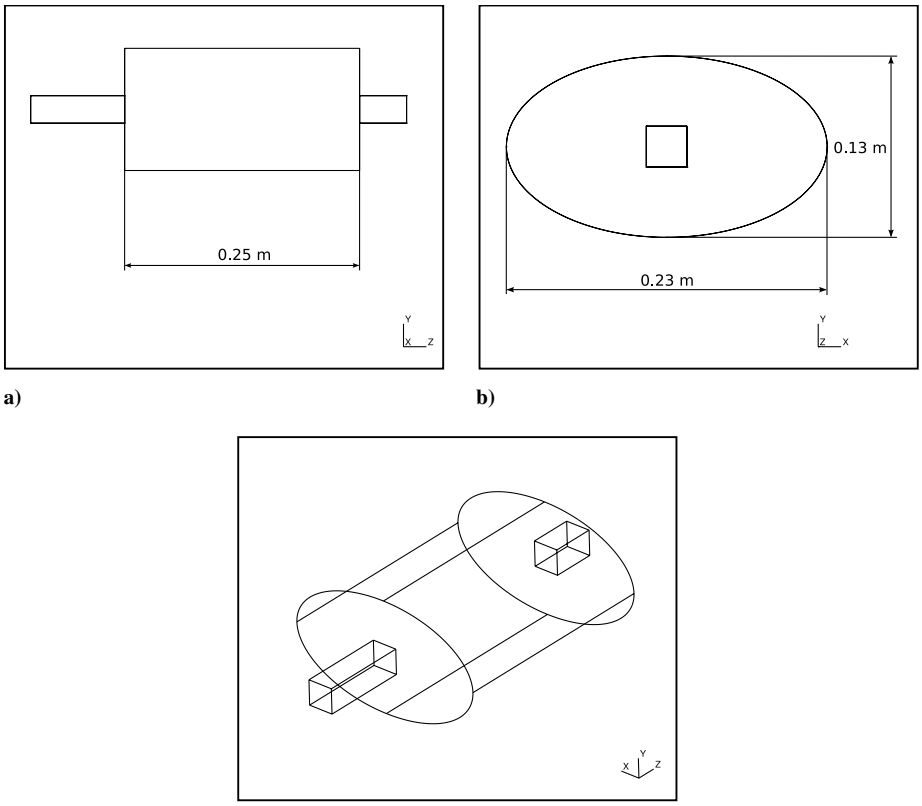

Fig. 13 Geometry for the muffler problem.

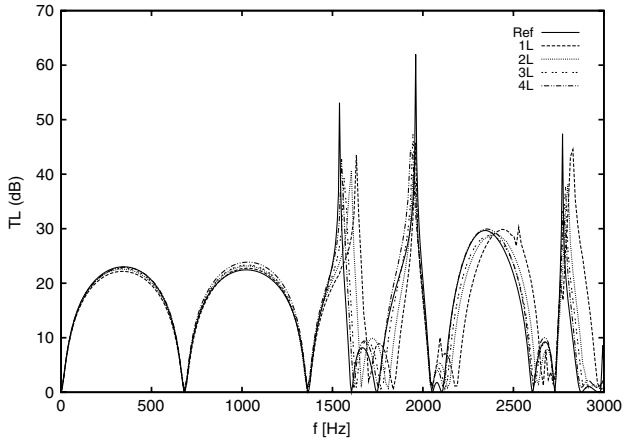

Fig. 14 Transmission loss for the muffler problem; effect of grid refinement.

transforms, these values are used to calculate the amplitude of right-traveling (p^+) and left-traveling (p^-) waves in the inlet and oulet ducts, assuming 1-D propagation (below the cut-off frequency of about 5800 Hz)

$$\begin{bmatrix} p^+_{\text{Inlet}} \\ p^-_{\text{Inlet}} \end{bmatrix} = \begin{bmatrix} e^{-ikz_1} & e^{ikz_1} \\ e^{-ikz_2} & e^{ikz_2} \end{bmatrix}^{-1} \cdot \begin{bmatrix} p_1 \\ p_2 \end{bmatrix}$$

$$\begin{bmatrix} p^+_{\text{Outlet}} \\ p^-_{\text{Outlet}} \end{bmatrix} = \begin{bmatrix} e^{-ikz_3} & e^{ikz_3} \\ e^{-ikz_4} & e^{ikz_4} \end{bmatrix}^{-1} \cdot \begin{bmatrix} p_3 \\ p_4 \end{bmatrix}$$

The transmission loss of the muffler is then computed as

$$\text{TL} = 20 \cdot \log\left(\frac{p^+_{\text{Inlet}}}{p^+_{\text{Outlet}}}\right)$$

Figure 14 shows the effect of grid refinement on the computed transmission loss. At lower frequencies the propagation through the chamber is longitudinal, so that it is not much affected by the discretization of the geometry. Resonances at 680 Hz, 1360 Hz, 2040 Hz, and 2720 Hz, corresponding to longitudinal modes, are captured by all grids. The geometry discretization strongly affects the simulation of transversal modes that appear above 1500 Hz, and only the finer grids yield accurate results over the whole frequency range considered.

The improvement in accuracy obtained by the use of the quadratic treatment on the coarsest grid (case 1Q) is shown in Fig. 15. The accuracy is comparable to that of the linear treatment applied to the finest grid (case 4L), whereas its computational cost is much lower, as shown in Table 12. In particular, the CPU time for case 1Q is about 4.4 times lower than for case 4L. As in the high-lift airfoil problem presented in Sec. III.B, the time step of all simulations is constrained

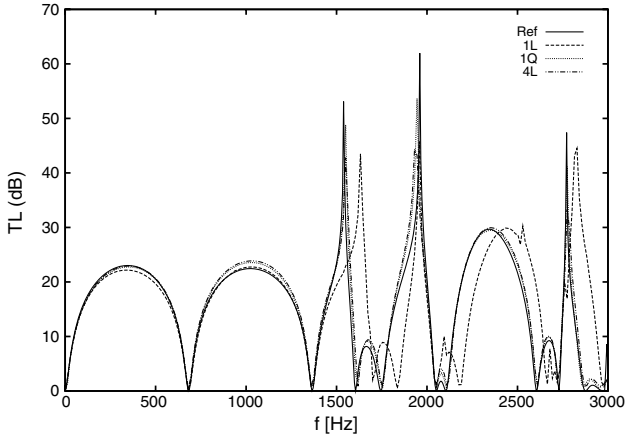

Fig. 15 Transmission loss for the muffler problem; comparison between linear and quadratic boundary treatment.

Table 11 Computation parameters used for the muffler problem

Test Case	Grid	p	Bnd. Treatment
1L	1	5	Linear
1Q	1	5	Quadratic
2L	2	5	Linear
3L	3	5	Linear
4L	4	4	Linear

Table 12 Time step and approximate computational cost for each computation of the muffler problem

Test Case	Time Step	CPU Time	Memory
1L	0.0012	41 min	8.5 MB
1Q	0.0012	42 min	21.0 MB
2L	0.0012	1 h 10 min	10.7 MB
3L	0.0011	2 h 48 min	17.3 MB
4L	0.0010	3 h 06 min	18.7 MB

by the geometry of the inlet and outlet ducts, where the smallest elements are located. The absence of such geometrical restrictions would make the combination of curved boundary treatments and coarse grids even more advantageous over grid refinement in terms of computation time.

IV. Conclusions

In this work, DGM is applied to the LEE on unstructured triangular and tetrahedral meshes to simulate aeroacoustic propagation. The quadrature-free form of DGM is used to achieve a low computational cost. The accuracy of the method can be efficiently controlled by freely specifying the order of the underlying polynomial basis, without affecting the compactness of the scheme.

The simulation of various 2-D and 3-D problems of acoustic propagation demonstrates that accuracy at high order can be limited by the linear treatment of curved geometries. The results of 2-D cases show that the mixed treatment consisting of prescribing wall boundary conditions with normals to the quadratic geometry, although integrating over elements with straight edges, is of limited interest for aeroacoustic applications. The full quadratic treatment involving curved elements proves successful to increase the accuracy with little additional computation cost for all test cases considered in this work.

The use of meshes featuring curved elements in the vicinity of curved wall boundaries allows to employ a uniform grid density over the whole computational domain, without excessive refinement near the geometry, and is thus necessary to fully benefit from the efficiency of high-order DGM. However, few methods for curved mesh generation are available today, and they still have to undergo development to reach satisfying standards in terms of robustness and grid quality. Moreover, curved elements affect the numerical behavior of DGM, with consequences on the stability conditions of explicit time integration schemes. The dependence of DGM on the element shape will be the subject of further investigations by the authors of this work, with the objective of defining grid quality metrics for meshing methods.

Acknowledgments

The authors are grateful to Frédéric Moens from Office National d'Études et de Recherches Spatiales for providing the geometry data of the high-lift airfoil. They wish to thank Jean–François Remacle (Université Catholique de Louvain) for his help with Gmsh and curved mesh generation, as well as Wim De Roeck (Katholieke Universiteit Leuven) for valuable discussions on the elliptical muffler problem. Thomas Toulorge acknowledges the financial support of the European Commission through the Marie Curie Research and Training network Aeroacoustical and Thermoacoustical Coupling in Energy Processes, contract number MRTN-CT-2006-035713.

References

[1] Reed, W. H., and Hill, T. R., "Triangular Mesh Methods for the Neutron Transport Equation," Los Alamos Scientific Lab., Technical Rept. LA-UR-73-479, 1973.

[2] Lesaint, P., and Raviart, P. A., "On a Finite Element Method for Solving the Neutron Transport Equation," *Mathematical Aspects of Finite Element in Partial Differential Equations*, Academic Press, New York, 1974.

[3] Atkins, H., and Shu, C.-W., "Quadrature-Free Implementation of the Discontinuous Galerkin Method for Hyperbolic Equations," *AIAA Journal*, Vol. 36, No. 5, 1998, pp. 775–782. doi:10.2514/2.436

[4] Hu, F. Q., and Atkins, H. L., "Two-Dimensional Wave Analysis of the Discontinuous Galerkin Method with Nonuniform Grids and Boundary Conditions," *8th AIAA/CEAS Aeroaoustic Conference*, AIAA, Reston, VA, 2002.

[5] Hu, F. Q., Hussaini, M. Y., and Rasetarinera, P., "An Analysis of the Discontinuous Galerkin Method for Wave Propagation Problems," *Journal of Computational Physics*, Vol. 151, No. 2, 1999, pp. 921–946. doi:10.1006/jcph.1999.6227

[6] Hagmeijer, R., Blom, C. P. A., and Hoeijmakers, H. W. M., "Wave-Speed Analysis of Discontinuous Galerkin Finite Element Method for Aeroacoustics," *ECCOMAS Computational Fluid Dynamics Conference 2001*, International Center for Numerical Methods in Engineering, Barcelona, Sept. 2001.

[7] Ainsworth, M., Monk, P., and Muniz, W., "Dispersive and Dissipative Properties of Discontinuous Galerkin Finite Element Methods for the Second-Order Wave Equation," *Journal of Scientific Computing*, Vol. 27, Nos. 1–3, 2006, pp. 5–40. doi:10.1007/s10915-005-9044-x

[8] Chevaugeon, N., Remacle, J.-F., Gallez, X., Ploumhans, P., and Caro, S., "Efficient Discontinuous Galerkin Methods for Solving Acoustic Problems," *11th AIAA/CEAS Aeroacoustics Conference*, AIAA, Reston, VA, Paper 2005-2823, 2005.

[9] Chevaugeon, N., Hillewaert, K., Gallez, X., Ploumhans, P., and Remacle, J.-F., "Optimal Numerical Parameterization of Discontinuous Galerkin Method Applied to Wave Propagation Problems," *Journal of Computational Physics*, Vol. 223, 2007, pp. 188–207. doi:10.1016/j.jcp.2006.09.005

[10] Reymen, Y., Baelmans, M., and Desmet, W., "Study of Convergence and Efficiency of a Nodal Quadrature-Free Discontinuous Galerkin Method on Meshes of Tetrahedral and Hexahedral Elements," *International Conference On Spectral and High Order Methods*, Global Science Press, Hong Kong, 2007.

[11] Reymen, Y., Baelmans, M., and Desmet, W., "On the Performance of the Quadrature-Free Discontinuous Galerkin Method on Hexahedral and Tetrahedral Grids for Linearized Euler Equations," *14th AIAA/CEAS Aeroacoustics Conference*, AIAA, Reton, VA, Paper 2008-3001, 2008.

[12] Hesthaven, J. S., and Warburton, T., "Nodal High-Order Methods on Unstructured Grids," *Journal of Computational Physics*, Vol. 181, 2002, pp. 186–221. doi:10.1006/jcph.2002.7118

[13] Blom, C. P. A., "Discontinuous Galerkin Method on Tetrahedral Elements for Aeroacoustics," Ph.D. Thesis, Univ. of Twente, Enschede, The Netherlands, 2003.

[14] Rao, P. P., "High Order Unstructured Grid Methods for Computational Aeroacoustics," Ph.D. Thesis, Pennsylvania State Univ., State College, PA, 2004.

[15] Dumbser, M., and Munz, C.-D., "ADER Discontinuous Galerkin Schemes for Aeroacoustics," *Comptes Rendus Mecanique*, Vol. 333, No. 9, 2005, pp. 683–687. doi:10.1016/j.crme.2005.07.008

[16] Delorme, P., Mazet, P., Peyret, C., and Ventribout, Y., "Computational Aeroacoustics Applications Based on a Discontinuous Galerkin Method," *Comptes Rendus Mecanique*, Vol. 333, No. 9, 2005, pp. 676–682. doi:10.1016/j.crme.2005.07.007

[17] Bassi, F., and Rebay, S., "High-Order Accurate Discontinuous Finite Element Solution of the 2D Euler Equations," *Journal of Computational Physics*, Vol. 138, No. 2, 1997, pp. 251–285.

doi:10.1006/jcph.1997.5454
[18] Krivodonova, L., and Berger, M., "High-Order Accurate Implementation of Solid Wall Boundary Conditions in Curved Geometries," *Journal of Computational Physics*, Vol. 211, No. 2, 2006, pp. 492–512.
doi:10.1016/j.jcp.2005.05.029
[19] Atkins, H. L., "Continued Development of the Discontinuous Galerkin Method for Computational Aeroacoustic Applications," AIAA, Reston, VA, Paper 97-1581, 1997.
[20] Reymen, Y., "3D High-Order Discontinuous Galerkin Methods for Time-Domain Simulation of Flow Noise Propagation," Ph.D. Thesis, Katolieke Universiteit Leuven, 2008.
[21] Carpenter, M. H., and Kennedy, C. A., "A Fourth-Order 2N-Storage Runge–Kutta Scheme," NASA TM 109112, 1994.
[22] Reymen, Y., Baelmans, M., and Desmet, W., "A 3D Discontinuous Galerkin Method for Aeroacoustic Propagation," *12th International Congress on Sound and Vibration*, International Institute of Acoustics and Vibration, Lisbon, 2005.
[23] Hesthaven, J. S., "From Electrostatics to Almost Optimal Nodal Sets for Polynomial Interpolation in a Simplex," *SIAM Journal on Numerical Analysis*, Vol. 35, No. 2, 1998, pp. 655–676.
doi:10.1137/S003614299630587X
[24] Geuzaine, C., and Remacle, J. F., "Gmsh: A Three-Dimensional Finite Element Mesh Generator with Built-In Pre- and Post-Processing Facilities," *International Journal for Numerical Methods in Engineering*, Vol. 79, No. 11, 2009, pp. 1309–1331.
[25] Tam, C. K. W., and Hardin, J. C. (Eds.), "Second Computational Aeroacoustics Workshop on Benchmark Problems," NASA Paper 3352, 1997.
[26] Toulorge, T., Reymen, Y., and Desmet, W., "A 2D Discontinuous Galerkin Method for Aeroacoustics with Curved Boundary Treatment," *Proceedings of the ISMA2008 Conference*, Katholieke Universiteit Leuven, Leuven, Belgium, 2008, pp. 565–578.
[27] Denia, F. D., Albelda, J., Fuenmayor, F. J., and Torregrosa, A. J., "Acoustic Behaviour of Elliptical Chamber Mufflers," *Journal of Sound and Vibration*, Vol. 241, No. 3, 2001, pp. 401–421.
doi:10.1006/jsvi.2000.3289
[28] Hong, K., and Kim, J., "Natural Mode Analysis of Hollow and Annular Elliptical Cylindrical Cavities," *Journal of Sound and Vibration*, Vol. 183, No. 2, 1995, pp. 327–351.
doi:10.1006/jsvi.1995.0257

J. Astley
Associate Editor